JOM, Vol. 68, No. 11, 2016
DOI: 10.1007/s11837-016-2094-8

Development of Cast Alumina-Forming Austenitic Stainless Steels

G. MURALIDHARAN,[1,2] Y. YAMAMOTO,[1] M.P. BRADY,[1] L.R. WALKER,[1] H.M. MEYER III,[1] and D.N. LEONARD[1]

1.—Materials Science and Technology Division, Oak Ridge National Laboratory, 1 Bethel Valley Road, Oak Ridge, TN 37831, USA. 2.—e-mail: muralidhargn@ornl.gov

Cast Fe-Ni-Cr chromia-forming austenitic stainless steels with Ni levels up to 45 wt.% are used at high temperatures in a wide range of industrial applications that demand microstructural stability, corrosion resistance, and creep strength. Although alumina scales offer better corrosion protection at these temperatures, designing cast austenitic alloys that form a stable alumina scale and achieve creep strength comparable to existing cast chromia-forming alloys is challenging. This work outlines the development of cast Fe-Ni-Cr-Al austenitic stainless steels containing about 25 wt.% Ni with good creep strength and the ability to form a protective alumina scale for use at temperatures up to 800–850°C in H_2O-, S-, and C-containing environments. Creep properties of the best alloy were comparable to that of HK-type cast chromia-forming alloys along with improved oxidation resistance typical of alumina-forming alloys. Challenges in the design of cast alloys and a potential path to increasing the temperature capability are discussed.

INTRODUCTION

Heat-resistant cast austenitic stainless steels are widely used as construction materials for process equipment in the chemical, heat-treating, metals processing, and petrochemical industries at temperatures up to 1150°C.[1] Examples of such alloys include HK-40 (Fe-25Cr-20Ni-0.4C), HP-40 (Fe-25Cr-35Ni-0.4C), and Fe-35Cr-45Ni-0.5C alloy, with higher temperatures requiring the use of higher Ni-alloys.[1–9] Creep resistance is achieved in these alloys through the formation of interdendritic MC and $M_{23}C_6$ carbides along with fine dispersions of carbides within the matrix.[2–9] These alloys rely on the formation of a chromia layer to achieve their oxidation resistance. Water vapor found in many industrially-relevant, chemical/petrochemical processing and energy conversion and combustion environments is known to accelerate the rate of oxidation, particularly for chromia-forming alloys since chromia is less stable than alumina in water vapor at high temperatures.[10,11] This accelerated degradation is driven in part by volatile Cr oxyhydroxide species and/or increased tendency for internal oxidation.[11–13]

Alumina-forming alloys exhibit superior high-temperature corrosion resistance compared to chromia-forming alloys in many highly aggressive, H_2O-, S-, and C-containing environments due to the slower growth rate and greater thermodynamic stability of alumina compared with that of chromia.[11–14] Development efforts for alumina-forming austenitics go back several decades.[15–19] Recent work has focused on the design of wrought alumina-forming austenitic stainless steels consisting of Fe-(12–14)Cr-(20–32)Ni-(2.5–4)Al-(0.6–2.5)Nb-(0.05–0.1)C (all in wt.%) alloys for use up to ~900°C.[20–22] To maximize the stability of the austenitic matrix, it was critical to limit the additions of ferrite stabilizers such as Cr, Al, and Nb in proportion to Ni-levels in the alloy (austenite stabilizer). Additions of both Cr and Al were found to be critical for the formation of a protective alumina scale, with additions of Al resulting in the precipitation of B2-NiAl which served as a source of Al. Nb additions promoted the formation of nanoscale MC-type carbides required for good creep resistance along with the Fe_2(Mo, Nb) Laves phase. It was hypothesized that Nb also promoted the formation of an external alumina scale at relatively lower levels of Cr and Al. In general, the optimum level of Nb for

(Published online September 6, 2016)

oxidation resistance was found to be in the range of 2.5–3 wt.% while optimal creep resistance was achieved with approximately 1 wt.% Nb.[22]

Development of cast alumina-forming alloys has been lagging behind that of wrought versions. Early work on cast versions of alumina-forming austenitic stainless steels typically utilized high levels of Cr (20–25 wt.% Cr) in combination with 20–45 wt.% Ni and targeted applications above 1000°C but with limited success.[23,24] Asteman et al.[25] highlighted the development of a Ni-based, Ni-Cr-Al cast alloy, Centralloy 60 HT R, an Al_2O_3 former for service at temperatures above 1000°C. This alloy was reported to contain Ni-(0–5) Fe-25Cr-4Al-3W-(0–0.5) Si-(0–0.5)Mn-0.4C and was strengthened by either secondary carbide or γ' formation depending on the Cr and Al levels. However, the promise of a lower-cost, cast Fe-based alumina-forming austenitic stainless steel has not yet been realized.

The goal of the present work was to evaluate the effect of alloy compositions on the creep properties and oxidation resistance of development grades of cast austenitic alloys designed to form an alumina-scale at temperatures up to 800–850°C. Since the formation of nanoscale MC-type carbides rich in Nb was found to be critical in achieving creep strength in wrought alumina-forming alloys,[20–22,26] an important objective of this study was to evaluate the effect of potential Nb partitioning and the formation of coarse interdendritic primary carbides during solidification on the creep properties of the cast alloys in this temperature range.

EXPERIMENTAL METHOD

An Fe-14Cr-25Ni-3.5Al-2Mn-2Mo-1W-0.5Cu alloy with additions of 0.1C-0.15Si-2.5Nb-0.01 wt.% B originally designed as an exemplary wrought alumina-forming alloy served as the base alloy for the cast alloy development process. Five developmental alloys, designated as Alloys 1–5 (compositions shown in Table I) were designed based on modifications to the base alloy.[27] Two different levels of Si (0.5 wt.% and 2 wt.%) were added, since Si is known to enhance castability by increasing the fluidity of the melt in Fe-based alloys. Alloys with two different Nb levels (1.0 wt.% and 2.5 wt.% Nb in the base alloy) were evaluated to understand the role of Nb on the creep and oxidation resistances of the alloys. It was hypothesized that the increased levels of Nb would allow more Nb to be retained within the matrix during solidification, thus providing enough Nb for the formation of nanoscale MC-type precipitates during high-temperature exposure. Four different carbon levels were considered (0.1 wt.% C, 0.2 wt.% C, 0.3 wt.% C, and 0.45 wt.% C) with the highest carbon levels being comparable to that of HK-type alloys (composition shown in Table I). Carbon levels were increased over the baseline alloy to compensate for the carbon that was expected to be tied up in the formation of primary carbides during solidification.

All alloys were arc-melted in an inert atmosphere in the form of buttons and then drop-cast into rectangular bars of size 13 × 25 × 150 mm in water-cooled copper hearths and tested in the as-cast condition. Creep tests were conducted at 750°C and at a stress of 100 MPa in air for all alloys, and additionally Alloy 4 was tested at 800°C at stress levels of 70 MPa and, at 650°C, 250 MPa. Sub-sized specimens with a gage length of 0.75″ (c.19 mm) and thickness of 0.125″ (c.3.2 mm) were used for creep testing. Specimens were cut with an electrical-discharge machine (EDM) and ground to a 600-grit (USA standard) finish.

Oxidation test samples 20 mm × 10 mm × (1–1.5) mm were EDM cut and polished to a 600-grit (USA standard) finish using SiC papers. Oxidation exposures were conducted in 100-h cycles at 800°C in air with 10 vol.% water vapor, with mass changes measured after every cycle (air cooling). Air was flowed through an alumina tube inside a resistively heated tube furnace, with distilled water added by atomization into the flowing gas stream above its condensation temperature (flow rates of 850 ml/min for air and 4.5–5.0 ml/h for water, furnace tube diameter of 5.5 cm). Test samples were positioned in alumina boats in the furnace hot zone so as to expose the sample faces parallel to the flowing gas. Further details can be obtained from.[28,29]

Elemental x-ray maps were acquired using a JEOL JXA-8200X electron microprobe analyzer (EPMA) instrument equipped with five crystal-focusing spectrometers for wavelength dispersive x-ray spectroscopy (WDS). WDS maps were acquired with an electron probe current of 200 nA. A Hitachi 3400 N SEM, operated at 15 kV and a working distance of 10 mm was also used to image samples in both secondary electron (SE) and back-scattered electron (BSE) modes. X-ray photoelectron spectroscopy (XPS) was conducted with a Thermo Scientific Model K-Alpha XPS instrument using a monochromated, micro-focusing, Al Kα x-ray source (1486.6 eV) with a 400-μm x-ray spot size for maximum signal and to obtain an average surface composition over the largest possible area. The oxidized sample was rinsed with ethanol and blown dry with compressed air prior to insertion into the XPS analysis chamber.

RESULTS AND DISCUSSION

Microstructure of As-Cast Alloys

Figure 1a and b shows the as-cast optical micrographs of the two alloys designated as base alloy and Alloy 1 in Table I, respectively. The size and spatial distribution of the dendrites are qualitatively comparable for these two alloys with approximate dendrite arm spacings of 10–20 μm. Figures 2, 3, and 4 show typical BSE images and

Table I. Chemical compositions in weight percent (wt.%) of vacuum arc-cast alloys analyzed by inductively coupled plasma and combustion techniques; also shown is the composition of a cast, chromia-forming austenitic stainless steel HK[29]

Name	ID	Fe	Cr	Mn	Ni	Cu	Al	Si	Nb	Mo	W	C	B	P	N (ppm)
HK		Bal.	25.6	0.93	18.1	0.06	–	1.68	0.19	0.35	0.07	0.45	NA	0.02	490
Base	OC4	49.1	13.9	1.94	25.2	0.50	3.47	0.15	2.49	2.00	1.00	0.09	0.006	0.019	5
Alloy 1	CAFA 1	49.7	14.0	1.92	25.1	0.51	3.56	0.94	0.95	1.98	0.99	0.20	0.009	0.020	5
Alloy 2	CAFA 2	48.3	14.0	1.94	25.2	0.51	3.46	0.93	2.42	1.98	0.98	0.22	0.010	0.016	17
Alloy 3	CAFA 3	48.8	14.1	1.97	24.9	0.51	3.51	2.04	0.89	1.98	0.90	0.19	0.012	0.019	11
Alloy 4	CAFA 4	49.9	14.1	1.92	25.3	0.51	3.49	0.48	0.94	1.98	1.00	0.29	0.008	0.020	12
Alloy 5	CAFA 6	49.3	13.9	1.95	25.5	0.48	3.51	0.98	0.88	1.99	0.97	0.45	0.008	0.003	4

All ORNL alloys contain 0.05 V and 0.05Ti. HK also contains 0.02 V, 0.09Co.

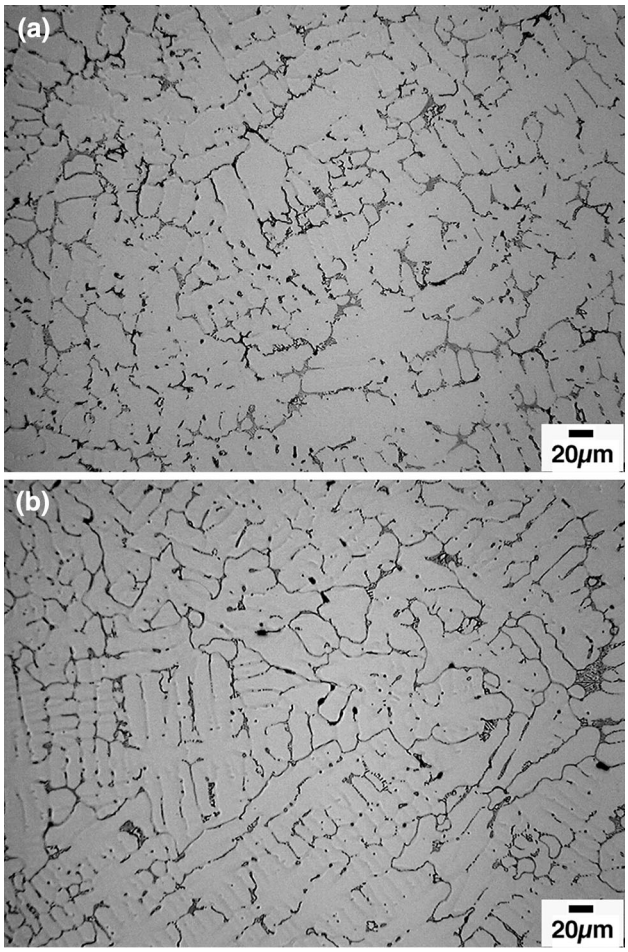

Fig. 1. Optical images of the as-cast microstructure of (a) base alloy and (b) Alloy 1. Alloy 1 shows a slightly finer microstructure with secondary dendrite arm spacings in both alloys being ~10–20 μm.

corresponding x-ray maps obtained from the as-cast microstructures of the base alloy, Alloy 1 and Alloy 4, respectively. Scheil and equilibrium calculations for 750°C were performed using nominal matrix compositions (excluding B, P, and N levels) to understand the microstructural evolution in the base and developmental alloys using JMatPro v.5.0.[30,31]

Microstructures and x-ray maps in Figs. 2, 3, and 4 clearly show Nb-enrichment and the presence of Nb-rich precipitates in the interdendritic regions. In the base alloy, two types of Nb-rich phases can be identified-a Nb-rich phase with carbon, inferred to be M (C, N)-type based upon the results of the calculations (Table II) and a second phase that shows Nb, Mo, Si, and W enrichment but without carbon. Calculations predict the presence of a Laves phase devoid of carbon, consistent with experimental observations. Figures 3 and 4 show that the interdendritic regions in Alloys 1 and 4 with higher nominal carbon levels consist predominantly of Nb-containing carbides M (C, N), consistent with calculations. In addition to the Nb-rich carbide, Alloy 1 shows the presence of islands of a carbide phase containing Mo, Si, W (shown in map), Fe and Cr (not shown). The microstructure of Alloy 4 also shows the presence of a Nb-rich carbide phase along with a second carbide phase similar to that observed in Alloy 1. The proportion of this phase increases from Alloy 1 to Alloy 4. Comparison of measured compositions with predicted calculations (particularly the presence of Si) suggests M_6C as the likely candidate.

Analyses of the matrix compositions using line profiles in the microprobe showed average levels of approximately 0.26 wt.% C, 1.1 wt.% Nb, 3.4 wt.% Al, 0.1 wt.% Si, and 15 wt.% Cr were present in the matrix in the base alloy. In contrast, similar measurements made in the matrix of Alloy 1 showed higher amount of carbon (0.37 wt.% C), a lower amount of Nb (0.4 wt.% Nb), and a slightly higher Al level (3.6 wt.%), higher Si levels (1 wt.% Si) consistent with higher nominal Si levels in the alloy compared to the base alloy, and 15 wt.% Cr. Matrix composition measurements in Alloy 4 also revealed high carbon levels (0.39 wt.% C), lower Nb levels (0.3 wt.% Nb), 3.6 wt.% Al, 1 wt.% Si and 14.7 wt.% Cr.

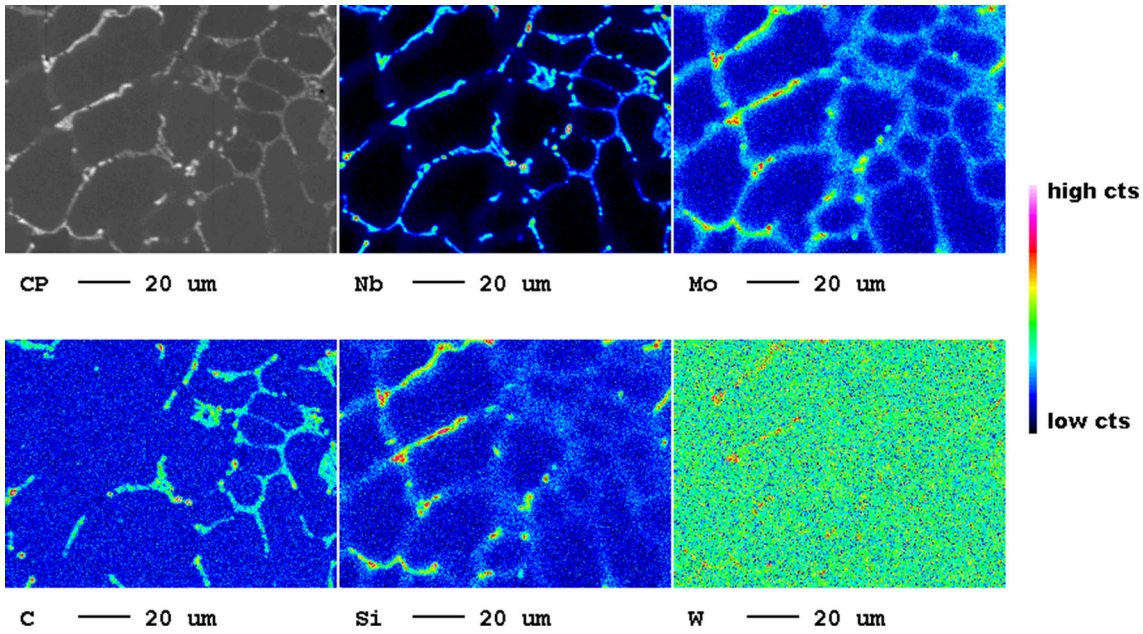

Fig. 2. Backscattered electron micrograph (CP), Nb (Lα), Mo (Lα), and C (Kα), Si (Kα), W (Mα) x-rays maps obtained from the base alloy in the as-cast condition.

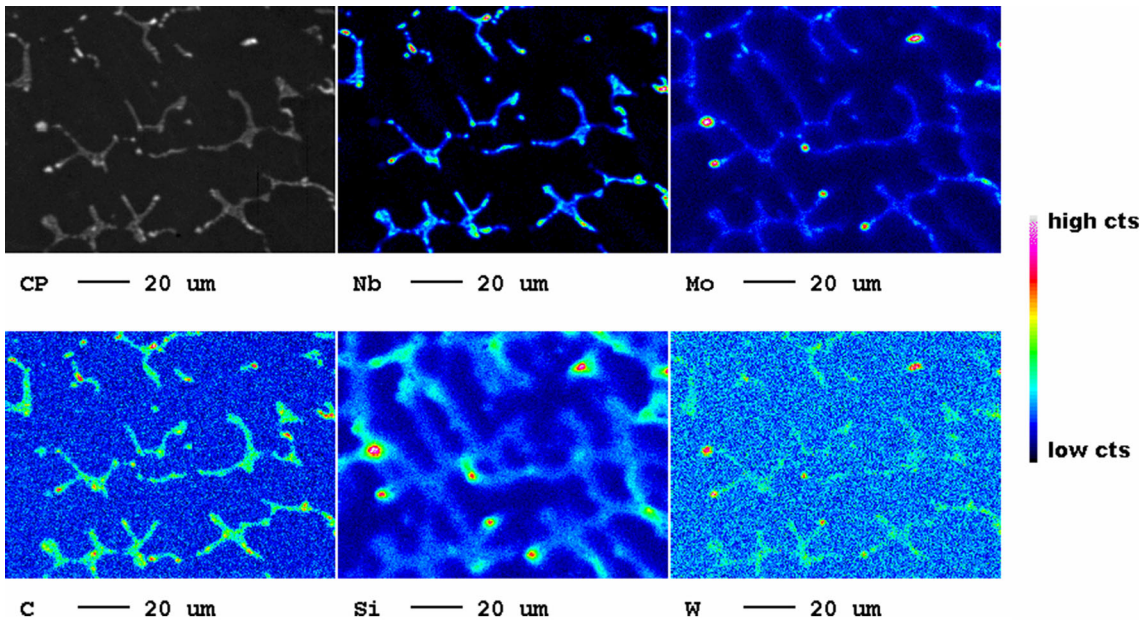

Fig. 3. Backscattered electron micrograph (CP), Nb (Lα), Mo (Lα), and C (Kα), Si (Kα), W (Mα) x-rays maps obtained from Alloy 1 in the as-cast condition.

Creep Resistance and Microstructural Evolution

Figure 5a shows that the creep rupture lives of the alloys at a stress level of 100 MPa at 750°C varied strongly with alloy composition. The cast base alloy exhibited a creep rupture life of ~500 h and the creep rupture lives for Alloy 2 and Alloy 3 were similar to that of the cast base alloy. This shows that the addition of Nb and Si to the base alloy did not result in any improvement in the creep properties. Alloys 1, 4, and 5 showed significantly better creep rupture lives when compared to the rupture life of the base alloy. Alloy 1 exhibited a lifetime of over 2000 h at 750°C and 100 MPa, Alloy

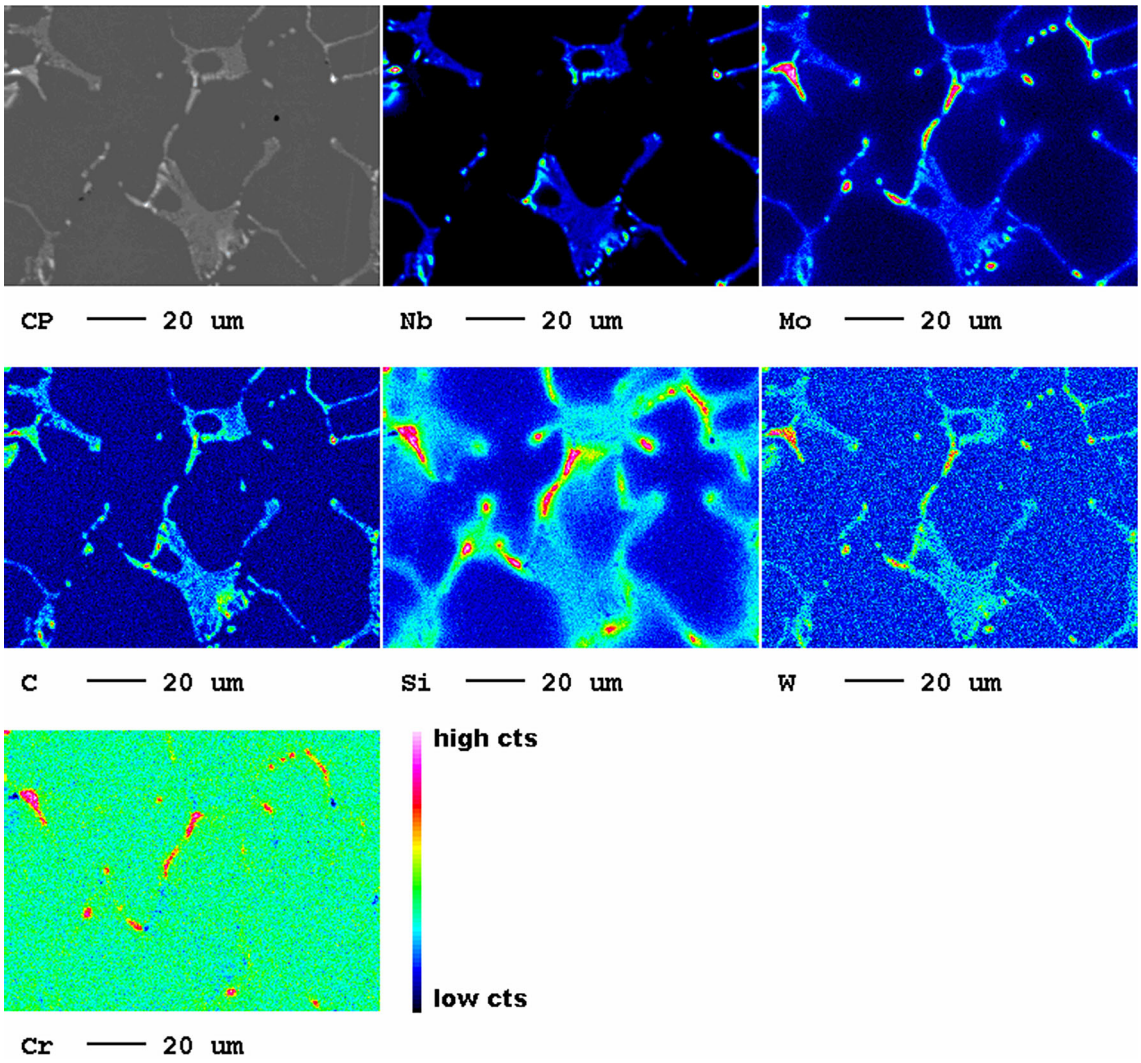

Fig. 4. Backscattered electron micrograph (CP), Nb (Lα), Mo (Lα), and C (Kα), Si (Kα), W (Mα), and Cr (Kα) x-rays maps obtained from Alloy 4 in the as-cast condition.

Table II. Predicted wt.% of phases present after solidification (Scheil calculations) and equilibrium wt.% of phases in various cast AFA alloys at 750°C

	B2-(Fe,Ni)Al		Laves		M(C, N)		$M_{23}C_6$		G-phase		
Cast alloys	**Scheil**	**Equ.**	**Scheil**	**Equ.**	**Scheil**	**Equ.**	**Scheil**	**Equ.**	**Scheil**	**Equ.**	**Others Scheil**
Base	1.5	9.2	2.5	5.0	0.7	0.9	–	–	–	–	
Alloy 1	0.3	9.9	0	2.9	0.9	0.7	0.0	2.8	–	–	0.8 (M_6C), 0.8 (ferrite)
Alloy 2	1.1	9.7	1.7	4.8	1.8	2.0	0.0	0.2	0.2	1.2	
Alloy 3	1.1	11.5	0.5	3.9	0.7	0.5	0.0	2.7	0.4	6.2	1.7 (M_6C), 0.3 (ferrite)
Alloy 4	0.0	7.9	0.0	3.2	0.9	0.7	0.4	2.7	0.0	0.0	0.3 (M_6C), 0.5 (ferrite)
Alloy 5	0.0	9.5	0.0	2.1	1.0	0.8	0.6	7.0	0.0	1.7	1.2 (M_6C), 1.4 (M_7C_3)

4 a lifetime of over 3500 h, and Alloy 5 a lifetime of over 10,000 h. A Larsen–Miller Parameter curve obtained from creep data for Alloy 4 in the temperature range of 650–800°C is shown in Fig. 5b along with the data for other developmental alloys at 750°C. This short-term data compare well with creep properties of a typical cast HK austenitic stainless steel obtained from the literature data

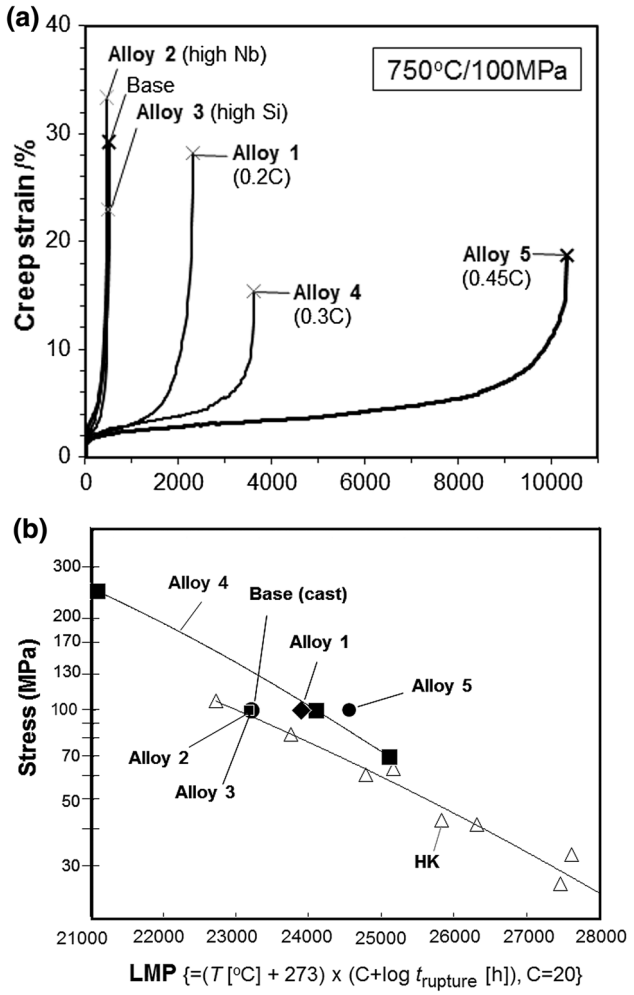

Fig. 5. (a) Time-dependent creep strain in various cast AFA alloys at 750°C, 100 MPa. (b) Larsen-Miller Parameter (LMP) plot comparing creep properties cast AFA alloys with that of HK-type alloys.

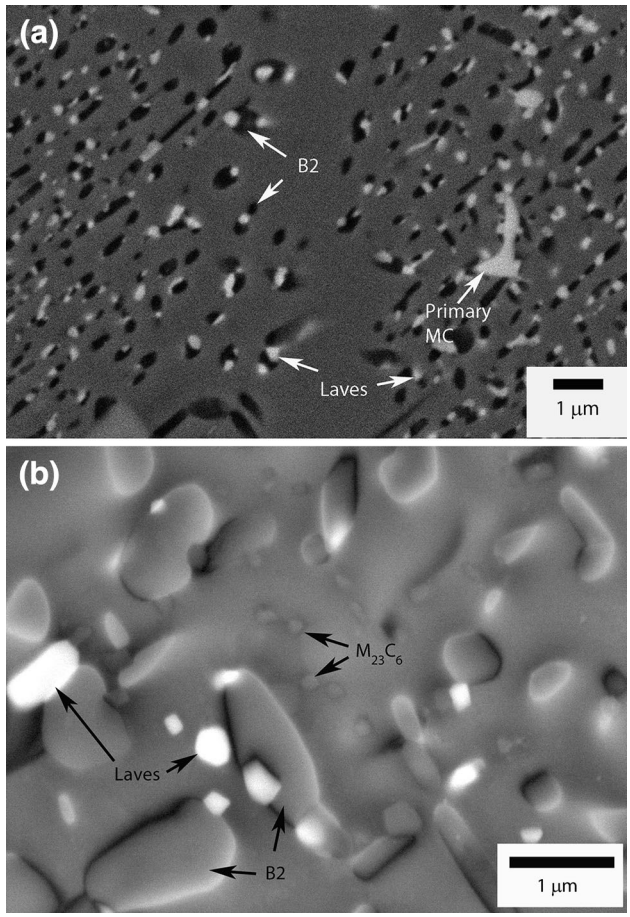

Fig. 6. Back-scattered scanning electron microscope image from alloys creep-tested to failure at 750°C, (a) base alloy, and (b) Alloy 5.

(test range of 760–982°C and up to 100,000 h rupture life).[1] Creep tests performed on a centrifugal cast version of Alloy 4 (CAFA7) confirmed this trend up to ~900°C,[32] but long-term creep tests are on-going.

Since all alloys were tested in the as-cast condition, the differences in creep rupture lives observed between the base alloy and Alloys 1, 4, and 5 is expected to be due to the differences in the second phase precipitation during creep testing. Figure 6a shows a BSE image from base alloy creep tested to failure at a temperature of 750°C (lifetime of 497 h). Comparison with the BSE image obtained in the as-cast condition, a copious precipitation of the dark phase [B2-(Fe,Ni)Al] associated with a bright globular phase (Fe_2Nb-Laves phase) within the grain interior can be observed. Larger MC-type carbides formed during solidification still remain, along with a small fraction of nanoscale carbides formed during exposure to 750°C. Some amount of fine MC-type carbide precipitation can be expected due to the Nb present in the matrix, but this amount will be restricted by carbon levels. This tendency for precipitation of fine MC-type carbides is indicated by the difference between the MC-type carbide contents predicted by the Scheil and equilibrium calculations in Table II.

Figure 6b shows a BSE image from Alloy 5 creep tested to failure at a temperature of 750°C (10,326 h exposure). In addition to the larger precipitates [B2-(Fe,Ni)Al, and Fe_2Nb-Laves phase], the presence of strings of small precipitates (< 100 nm in size) with contrast similar to that of the matrix was identified. Transmission electron microscopy work suggests the presence of $M_{23}C_6$ which is likely to be responsible for the improved creep properties of these alloys. Since the Nb levels in the matrix were much lower than the base alloy in the as-cast condition with much higher C levels, there is a greater tendency for non-MC-type carbides to precipitate during high-temperature exposure. Equilibrium calculations suggest a larger fraction of $M_{23}C_6$ at 750°C compared to the base alloy and Alloys 1–4. The good creep properties of HK-40 between 750°C and 1000°C were attributed to the presence of a high number density of fine $M_{23}C_6$ precipitates,[2] and $M_{23}C_6$-type carbides were identified in HP-Nb alloys subject to long-term service.[33] Faster

coarsening of $M_{23}C_6$ was considered as detrimental to creep resistance at temperatures of 1000°C or higher in HK-type alloys,[3] and thus could be a factor in the use of current series of alloys at 1000°C or higher. The precipitation of G-phase predicted in Alloy 3 containing nominally 2 wt.% Si and lower Nb levels may be responsible for the lower creep rupture live observed in Alloy 3 when compared to Alloys 1,4, and 5 as shown in Fig. 5a.

Oxidation Behavior

Figure 7a shows the specific mass changes observed as a function of time during oxidation testing of the base alloy and other developmental alloys at 800°C in air with 10 vol.% water vapor (data obtained in 100-h cycles). Included for comparison are data from chromia-forming cast HK (20 wt.% Ni) which shows mass loss in this testing condition due to volatile Cr oxyhydroxide species.[11–13,34] Depending on the alloy composition (especially Ni and Cr levels),[34] exposure time, temperature, water vapor content, and sample thickness, Fe-based chromia-forming alloys suffer from accelerated transition to the formation of a nonprotective Fe-based oxide formation (observed at ~3000 h for alloy HK at 800°C in air + 10% H_2O in Fig. 7b).[29]

In contrast, the base AFA alloy and the new cast AFA Alloy 4[29] showed low, positive specific mass gains (<0.5 mg/cm^2 after 5000 h) consistent with protective alumina scale formation in the range of a few microns thick (confirmed by cross-section analysis, see Ref. 29 for further details). Figure 7b shows an XPS depth profile for Alloy 4 after 5000 h at 800°C in air + 10% water vapor. The scale was found to consist primarily of Al and O, with only minor amounts of Cr, Fe, Mn, and Nb (Ni was not detected at the outer surface and was therefore not tracked in this profile data). Alloy 1, which contained 0.2 wt.% C compared with 0.3 wt.% C in Alloy 4, exhibited slightly higher but still low positive mass change of approximately 0.6 mg/cm^2 after 2500 h of testing evaluated for this alloy, again indicative of protective alumina scale formation. Increasing the C level to 0.45 wt.% C in Alloy 5 moderately increased the oxidation rate, and resulted in an approximate positive mass gain of 1.5 mg/cm^2 after 4000 h, suggesting an alloy composition approaching the borderline for protective alumina scale formation at 800°C in air with 10% water vapor. The present findings suggest that C levels of 0.3-0.4 wt.% C are required to balance creep properties with oxidation resistance.

Oxidation tests in air at 900°C on a centrifugally cast alloy derived from composition of Alloy 4 showed early indications of local internal attack after a 2000-h exposure.[32] This suggests that cast AFA alloys in this composition range with approximately 25 wt.% Ni are restricted to maximum operating temperatures of 800–850°C depending on the water vapor levels in the environment. Preliminary results suggest that cast AFA alloys capable of alumina formation up to 1100°C can be achieved using a similar design philosophy but with higher levels of Ni and Cr along with reactive element additions.[32] Further work on evaluating the oxidation resistance and creep properties of centrifugal cast alloys with modified compositions is on-going.

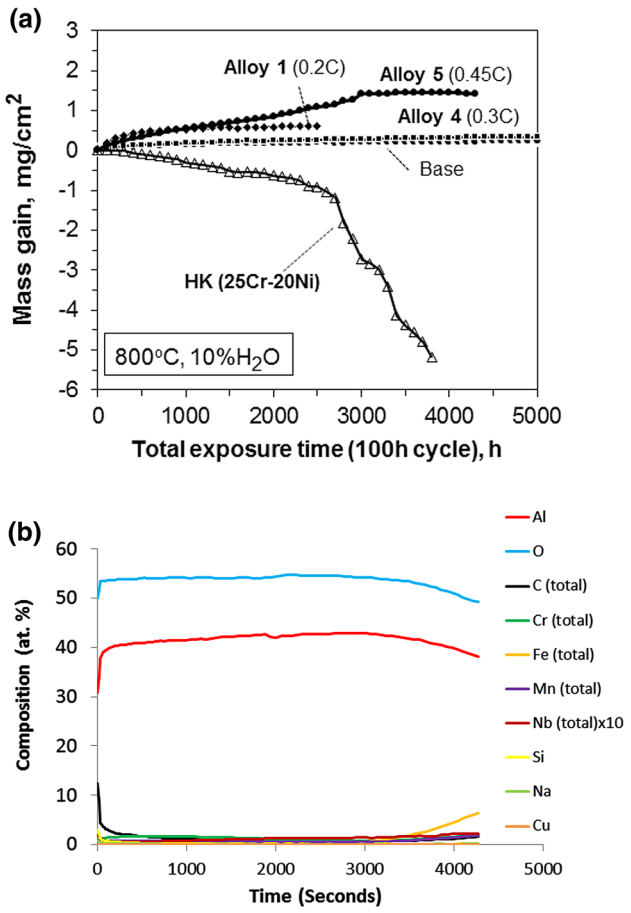

Fig. 7. (a) Specific mass change at 800°C in air with 10% H_2O (100-h cycles) for several alumina-forming cast alloys and cast chromia-forming alloy HK (HK and Alloy 4 data from).[29] (b) Elemental distribution in an XPS depth profile for Alloy 4 after 5000 h at 800°C in air + 10% water vapor. Sputtering was performed using 2-kV Ar ions with an ion current sufficient to remove material at a rate of ~13 nm/min in a 100-nm-thick SiO_2 standard.

CONCLUSION

The effects of alloy composition on the microstructure, creep, and oxidation behavior of several developmental cast alumina-forming austenitic stainless steels containing approximately 25 wt.% Ni-14 wt.% Cr-3.5 wt.% Al and with varying levels of Nb, Si, and C were evaluated. Although electron microprobe results show that Nb-partitioning occurs during solidification, good creep and oxidation resistance are achieved in alloys with

approximately 1.0 wt.% Nb, 1.0 wt.% Si and 0.3–0.4 wt.% C. Improved creep properties at these Nb and C levels can be attributed to the presence of $M_{23}C_6$-type carbides in addition to Nb-rich MC-type carbides. The newly developed cast AFA alloys show improved oxidation performance compared to HK-type chromia-forming alloy without compromising creep properties at temperatures up to about 800–850°C. Alloys with higher Ni and Cr levels are being developed to overcome local internal attack observed in centrifugally cast alloys within this composition range at 900°C and higher temperatures.

ACKNOWLEDGEMENTS

Research sponsored by the US Department of Energy, Office of Energy Efficiency and Renewable Energy, Advanced Manufacturing Office, the Technology Innovation Program at Oak Ridge National Laboratory, and ARPA-E under Contract DE-AC05-00OR22725 with UT-Battelle, LLC.

REFERENCES

1. *Steel Castings Handbook, Supplement 9, High Alloy Data Sheets: Heat Series* (Crystal Lake, IL: Steel Founders' Society of America, 2004), pp. 2–60.
2. H. Wen-Tai and R.W.K. Honeycombe, *Mater. Sci. Technol. Ser.* 1, 385 (1985).
3. H. Wen-Tai and R.W.K. Honeycombe, *Mater. Sci. Technol. Ser.* 1, 390 (1985).
4. G.D. Barbabela, L.H. de Almeida, T.L. da Silveira, and I. Le May, *Mater. Charact.* 26, 1 (1991).
5. G.D. Barbabela, L.H. de Almeida, T.L. da Silveira, and I. Le May, *Mater. Charact.* 26, 193 (1991).
6. G.D. Barbabela, L.H. de Almeida, T.L. da Silveira, and I. Le May, *Mater. Charact.* 29, 387 (1992).
7. C.W. Thomas, M. Borshevsky, and A.N. Marshall, *Mater. Sci. Technol. Ser.* 8, 390 (1992).
8. R.A.P. Ibanez, G.D. de Almeida Soares, L.H. de Almeida, and I. Le May, *Mater. Charact.* 30, 243 (1993).
9. I.A. Sustaita-Torres, S. Haro-Rodriguez, M.P. Guerrero-Mata, M. de La Garza, E. Valdes, F. Deshcaux-Beaume, and R. Colas, *Mater. Chem. Phys.* 133, 1018 (2012).
10. E.J. Opila, *Mater. Sci. Forum* 461–464, 765 (2004).
11. E.J. Opila, N.S. Jacobson, D.L. Myers, and E.H. Copland, *JOM* 58, 22 (2006).
12. W.J. Quadakkers, J. Zurek, and M. Hansel, *JOM* 61, 44 (2009).
13. S.R.J. Saunders, M. Monteiro, and F. Rizzo, *Prog. Mater. Sci.* 53, 775 (2008).
14. F.H. Stott, G.C. Wood, and J. Stringer, *Oxid. Met.* 44, 113 (1995).
15. T. Fujioka, M. Kinugasa, S. Iizumi, S. Teshima, I. Shimizu, US Pat. # 3,989,514, (1976).
16. J.A. McGurty, US Pat. # 4,086,085, (1978).
17. D. Satyanarayana, G. Malakondaiah, and D. Sarma, *Mater. Sci. Eng., A* 323, 119 (2002).
18. V. Ramakrishnan, J.A. McGurty, and N. Jayaraman, *Oxid. Met.* 60, 185 (1988).
19. B.A. Pint, R. Peraldi, and P.J. Maziasz, *Mater. Sci. Forum* 461–464, 815 (2004).
20. Y. Yamamoto, M.P. Brady, Z.P. Lu, P.J. Maziasz, C.T. Liu, B.A. Pint, K.L. More, H.M. Meyer, and E.A. Payzant, *Science* 316, 433 (2007).
21. Y. Yamamoto, M.P. Brady, Z.P. Lu, C.T. Liu, M. Takeyama, P.J. Maziasz, and B.A. Pint, *Metall. Mater. Trans. A* 38A, 2737 (2007).
22. Y. Yamamoto, M.P. Brady, M.L. Santella, H. Bei, P.J. Maziasz, and B.A. Pint, *Metall. Mater. Trans. A* 42A, 922 (2011).
23. J.C. Pivin, D. Delaunay, S. Roquescarmes, A.M. Huntz, and P. Lacombe, *Corros. Sci.* 20, 351 (1980).
24. N. Belen, P. Tomaszewicz, and D.J. Young, *Oxid. Met.* 22, 227 (1984).
25. H. Asteman, W. Hartnagel, and D. Jakobi, *Oxid. Met.* 80, 3 (2013).
26. D.Q. Zhou, W.X. Zhao, H.H. Mao, Y.X. Hu, X.Q. Xu, X.Y. Sun, and Z.P. Lu, *Mater. Sci. Eng., A* 622, 91 (2015).
27. G. Muralidharan, Y. Yamamoto, and M.P. Brady, US Patent # 8,431,072, (2013).
28. B.A. Pint, J.P. Shingledecker, M.P. Brady, and P.J. Maziasz, in *Proceedings of GT2007 ASME Turbo Expo 2007: Power for Land, Sea, and Air.* May 14–17 (Montreal, Canada, 2007), 3, 995 (2007).
29. M.P. Brady, G. Muralidharan, D.N. Leonard, J.A. Haynes, R.G. Weldon, and R.D. England, *Oxid. Met.* 82, 359 (2014).
30. N. Saunders, X. Li, A.P. Miodownik, and J.-Ph. Schillé, *Materials Design Approaches and Experiences*, ed. J.-C. Zhao, M. Fahrmann, and T.M. Pollock (Warrendale, PA: TMS, 2001), pp.185–197.
31. N. Saunders, Fe-DATA, a database for thermodynamic calculations for Fe-Alloys. Thermotech Ltd., Surrey Technology Centre, The Surrey Research Park, Guilford, Surrey, GU2 7YG, UK.
32. G. Muralidharan, Y. Yamamoto, M.P. Brady, B.A. Pint, D. Voke, and R.I. Pankiw, *Corrosion 2015, Paper 6114* (Houston: NACE International, 2015).
33. S. Shi and J.C. Lippold, *Mater. Charact.* 59, 1029 (2008).
34. R. Peraldi and B.A. Pint, *Oxid. Met.* 61, 463 (2004).